

The role of fluctuations in quantum and classical time crystals

Toni L. Heugel,¹ Alexander Eichler,² R. Chitra,¹ and Oded Zilberberg³

¹*Institute for Theoretical Physics, ETH Zürich, CH-8093 Zürich, Switzerland.*

²*Laboratory for Solid State Physics, ETH Zürich, CH-8093 Zürich, Switzerland.*

³*Department of Physics, University of Konstanz, 78464 Konstanz, Germany.*

(Dated: March 14, 2022)

Discrete time crystals (DTCs) are a many-body state of matter whose dynamics are slower than the forces acting on it. The same is true for classical systems with period-doubling bifurcations. Hence, the question naturally arises what differentiates classical from quantum DTCs. Here, we analyze a variant of the Bose-Hubbard model, which describes a plethora of physical phenomena and has both a classical and a quantum time-crystalline limit. We study the role of fluctuations on the stability of the system and find no distinction between quantum and classical DTCs. This allows us to probe the fluctuations in an experiment using two strongly coupled parametric resonators subject to classical noise.

I. INTRODUCTION

The study of many-body periodically driven systems has experienced a boost in activity over recent years with the advent of discrete time crystals (DTCs) [1–21]. These are systems that respond to an external drive (at frequency ω_G) and fulfill the following three criteria: (i) The period of the response is subharmonic at an integer multiple of that of the drive, or equivalently, its response frequency ω is an integer fraction of ω_G , $\omega = \omega_G/n$ with n integer; (ii) in its own rotating frame at ω , the system appears to be stationary and exhibits long-time stability. In particular, no decay to a different state should occur when the system size approaches the thermodynamic limit; and (iii) The system exhibits sufficiently long-ranged correlations.

Much discussion is currently focused on the necessary and sufficient conditions to fulfill the three criteria listed above [22–27]. For example, discrete time-translation symmetry breaking (DTTSB) leading to (i) has long been known in the field of nonlinear dynamics and is, for instance, a prominent phenomenon in Kerr Parametric Oscillators (KPOs) [28–33]. In this context, the many-body aspect (iii) naturally emerges from the existence of normal modes for both weak and strong coupling between local degrees of freedom [34]. However, KPOs are inherently open systems, leading to unresolved questions in their ability to maintain criterion (ii), in the presence of dissipation and decoherence [16, 26, 35–40]. These questions are intricately linked to the degree of coherence that can be achieved in any driven phase of matter. Examining the role played by fluctuations leads to a very basic question: in what sense does a quantum DTC differ from a classical one?

In this paper, we answer this question by showing that the key features characterizing a quantum DTC can be recovered within a purely classical and dissipative setting. We start from a Bose-Hubbard variant of a driven quantum many-body system [11, 41–43] and elucidate the role of dissipation and nonlinearity for its stationary behavior. We observe that the quantum many-body sys-

tem forms normal modes [fulfilling (i) and (iii)] with DTC phases that mix over time through quantum fluctuations. This implies that criterion (ii) is only fulfilled for short and intermediate times, and that the DTC is by definition “prethermal” [3, 44, 45]. Interestingly, the steady state mixes only between different DTC phases, which may lead to signatures of the subharmonic response also in the long-time limit. We then compare the full quantum treatment with a mean-field picture, and investigate the quantum fluctuations of the DTC. Finally, we present a simple and classical experimental realization of a dissipative DTC and compare the quantum predictions to the measured results. Surprisingly, all the crucial aspects of the long-time behavior of the quantum model can be found in the classical experiment, demonstrating unambiguously that classical and quantum DTC share the same basic properties. Our treatment highlights that condition (ii) is much easier to fulfill in a classical system as the large amplitudes are more resilient to fluctuations, leading to a somewhat counter-intuitive “classical superiority” for DTC physics.

II. QUANTUM MANY-BODY TREATMENT

We begin by investigating DTTSB in a many-body closed quantum system, i.e., we identify its time-crystalline phases. Our starting point is a N -site network of interacting bosonic nodes subject to a homogeneous two-photon drive

$$H(t) = \sum_j \hbar \left[\omega_j a_j^\dagger a_j + \frac{V_j}{12} (a_j^\dagger + a_j)^4 - e^{i\omega_G t} \frac{G_j}{2} a_j^\dagger a_j^\dagger - e^{-i\omega_G t} \frac{G_j^*}{2} a_j a_j + \sum_{k \neq j} \frac{J_{jk}}{2} (a_j^\dagger + a_j)(a_k + a_k^\dagger) \right], \quad (1)$$

where a_j annihilates a bosonic particle (photon) on the j^{th} site with respective eigenenergy ω_j and Duffing nonlinearity V_j , see Fig. 1(a) for a 2D example. The resonators are all-to-all coupled with amplitudes J_{jk} and are

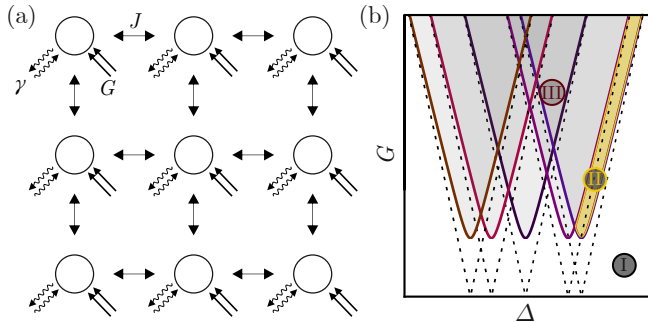


FIG. 1: (a) An example of a 2D graph of coupled parametric oscillators. They are nearest-neighbour coupled with amplitude J and are subject to a homogeneous two-photon (parametric) drive G , and damping γ , cf. Eq. (1). (b) Parametric instability lobes of normal modes: the linear system is unstable under the parametric drive whenever the drive amplitude exceeds a normal-mode threshold, cf. Eqs. (3) and (4). Dashed lines are used for the closed system and solid lines with shaded regions for the open system (6).

driven with two-photon (squeezing, parametric) drives with amplitudes G_j at a homogeneous drive frequency ω_G .

Moving to a frame rotating at half the parametric two-photon driving frequency, i.e., by using the unitary transformation $e^{-i\sum_j a_j^\dagger a_j \omega_G t/2}$ and taking the rotating-wave approximation, we obtain an effective Hamiltonian of a N -site variant of the Bose-Hubbard model subject to two-photon squeezing terms, or equivalently N coupled KPOs [43],

$$\bar{H} = \hbar \sum_j \left[-\Delta_j a_j^\dagger a_j + \frac{V_j}{2} a_j^\dagger a_j^\dagger a_j a_j - \frac{G_j}{2} a_j^\dagger a_j^\dagger - \frac{G_j^*}{2} a_j a_j + \sum_{k \neq j} \frac{J_{jk}}{2} (a_j^\dagger a_k + a_j a_k^\dagger) \right], \quad (2)$$

with linear detunings $\Delta_j = \omega_G/2 - \omega_j - V_j$. Note that a more precise rotating approach exists [46], but the standard rotating frame suffices for our discussion here and appeals to a larger audience.

Coupled harmonic oscillators form normal modes. Therefore, by neglecting the parametric drive and Kerr nonlinearities, we can diagonalize Eq. (2) in a normal mode basis

$$H_{nm} = \sum_k \hbar \tilde{\Delta}_k b_k^\dagger b_k, \quad (3)$$

where b_k denotes a linear combination of a_j with detuning $\tilde{\Delta}_k$ of the k^{th} normal mode. In this limit, our system appears to be composed of N decoupled harmonic oscillator modes. We can apply the same normal-mode transformation also in the driven and nonlinear case. The role of the Kerr terms V_j in the normal-mode basis is not trivial: the Kerr nonlinearities generate self-Kerr terms V_k

for each normal mode, and cross-normal-mode nonlinear couplings [47, 48]. Nevertheless, for weak nonlinearities and low-photon numbers, we can neglect the cross terms to obtain approximately a system of N decoupled normal modes with corresponding normal-mode Kerr terms.

The parametric drives in the normal basis give rise to eigenmode- and two-mode squeezing terms

$$H_{nm}^G = \hbar \sum_k \frac{\tilde{G}_{kk}}{2} b_k^\dagger b_k^\dagger + \hbar \sum_{l \neq k} \frac{\tilde{G}_{lk}}{2} b_l^\dagger b_k^\dagger + \text{h.c.}, \quad (4)$$

appearing as the terms containing \tilde{G}_{kk} and \tilde{G}_{lk} , respectively. In our rotating picture, the former terms are important for DTTSB: they lead to instability lobes for the normal modes whenever the two-photon drive amplitude hits parametric resonance, i.e., whenever the system crosses the instability threshold $|\tilde{\Delta}_j| = |\tilde{G}_{jj}|$ of one of the normal modes, see Fig. 1(b) [49, 50]. Below this threshold, the two-photon drive does not excite the system and no time-crystalline phase is formed, see regime I in Fig. 1(b). Beyond this instability threshold, however, the modes undergo a DTTSB, where the system's normal-mode Kerr nonlinearity prevents the absorption of infinitely-many photons from the drive and stabilizes the so-called time crystal [11, 34].

In ‘regime II’, we indeed observe that the N -coupled resonators are best described by our (approximate) construction of a parametrically driven (collective) normal mode that undergoes a spontaneous \mathbb{Z}_2 DTTSB, see Fig. 1(b) [34]. However, moving away from this regime by increasing the parametric drive or detuning, our approximations are no longer valid, and we expect that the cross-Kerr coupling and two-mode squeezing terms couple the normal modes. In this ‘regime III’, the DTTSB involves a larger number of DTTSB solutions, leading to a richer phase diagram [47]. Note that the latter regime involves the interplay of many normal modes that undergo DTTSB with a large overlap in the Δ - G parameter space [34]. Hence, there are two possible interpretations of many-body time crystals: on the one hand, one may be satisfied with a single collective mode that undergoes DTTSB, as in the fundamental mode of a massive mechanical resonator composed of many atoms [51, 52], or a row of strongly coupled pendula [47, 53]. On the other hand, one can demand that N collective modes undergo DTTSB and their mutual interaction leads to new time-crystalline phases. The second case relies on weak coupling (or stronger driving) to allow for overlapping normal modes [34]. Both interpretations fulfill criteria (i) and (iii).

Now, we turn to discuss when criterion (ii) is fulfilled. As long as our approximate reasoning holds (regime II), each normal mode evolves coherently in its ‘cat-qubit’ basis [54, 55] while being locked to half the frequency of the drive. This means that in this pure quantum limit, we will have a superposition of normal-mode DTCs. Depending on the initial conditions of the system and for carefully chosen Δ and J -values, we could fulfill crite-

tion (ii). Realistically, however, we will observe coherent oscillations between the DTCs that will average out in the long-time limit. Moreover, moving away from the decoupled pure quantum regime by relaxing our approximations, the inter-mode terms will couple the different normal-mode DTCs. Such terms can either lead to new DTC phases [47] in the strong coupling limit, or weak mixing between the existing normal-mode DTCs. In both cases, we will observe an increased mixing between states, leading to loss of criterion (ii). Interestingly, as we will see below, the mixing exclusively involves states manifesting DTTSB even in the long-time limit.

So far, we dealt with a closed quantum system. Some parts of the closed system act as a bath to the normal modes that undergo DTTSB, thus limiting the duration wherein criterion (ii) is fulfilled. We now explicitly consider coupling to a zero-temperature dissipative environment resulting in weak single-photon loss terms at each site modeled as Lindblad dissipators

$$\mathcal{L}[\hat{O}]\rho = 2\hat{O}\rho\hat{O}^\dagger - \left\{ \hat{O}^\dagger\hat{O}, \rho \right\}, \quad (5)$$

with associated rates $\gamma_j \ll \omega_0$. The time evolution of the system's density matrix ρ is given by

$$\dot{\rho} = -\frac{i}{\hbar}[H, \rho] + \sum_l \frac{\gamma}{2} \mathcal{L}[a_l]\rho, \quad (6)$$

where dots indicate time derivatives and $\gamma_j \equiv \gamma$. In Eq. (5), the anti-commutator term corresponds to dissipation, while the other so-called *recycling* or *quantum jump* term encodes fluctuations and ensures the normalization $\text{Tr}\rho \equiv 1$ of the system's density matrix. Crucially, opening the system to weak dissipation channels solely pushes the boundaries of the aforementioned instability lobes and slightly modifies the corresponding phase diagram [50, 56], see Fig. 1(b). Linear damping cannot compensate for the 'exponential' two-photon driving term [50, 54, 56]. Hence, we emphasize that the time-crystalline phases are still stabilized by the nonlinearity, and that there is no fundamental difference between dissipative and non-dissipative DTCs. Yet, as we shall now see, even at zero temperature, the bath-induced quantum fluctuations will mix DTCs and limit the duration in which criterion (ii) prevails.

III. EXAMPLE WITH $N = 2$

To illustrate the time-crystalline phases discussed above, we numerically solve the Lindblad master equation (6) for stationary distributions using QuTiP [57] for the case of two identical oscillators ($\Delta_j = \Delta$, $V_j = V$, $G_j = G$, and $J_{jk} = J$ with $j \neq k$), see Fig. 2(a). Here, we expect in the linear limit to only have a single symmetric (S) and a single antisymmetric (A) normal mode, at detunings $\Delta = \pm J$ with associated parametric instabilities at $|G| \geq \sqrt{(\Delta - J)^2 + (\gamma/2)^2}$ and

$|G| \geq \sqrt{(\Delta + J)^2 + (\gamma/2)^2}$, respectively, cf. solid lines in Fig. 2(b).

In Figs. 2(c)-(e), we present the joint probability distribution $\langle x_1, x_2 | \rho_s | x_1, x_2 \rangle$ obtained when measuring $(x_1, x_2) \equiv (a_1 + a_1^\dagger, a_2 + a_2^\dagger)/\sqrt{2}$ simultaneously on the unique stationary ρ_s . In Fig. 2(c), representative for regime I, we see that the distribution below the instability threshold is centered around $x_1 = x_2 = 0$. Moving beyond the threshold of the symmetric normal mode, we obtain an example of regime II in Fig. 2(d): both sites are displaced and we observe a \mathbb{Z}_2 symmetry-breaking for the symmetric mode (S-state). A similar scenario is observed slightly above the threshold of the antisymmetric mode (A-state) [47]. By moving away from the weak parametric instability threshold, we enter regime III and observe that additional time-broken phases appear in the stationary distribution of our system, dubbed mixed-symmetry states (M-states), see Fig. 2(e). Depending on the system parameters, we find various such mixtures of states [47].

The system is driven at ω_G and we observe "hot spots" of distinct oscillation modes moving at $\omega_G/2$, which is the signature of a DTTSB. However, quantum fluctuations lead to a sampling around and mixing between the DTTSB regions of phase space. Thus, after long times, the system approaches a "thermalized" distribution that mixes between different time-crystalline states, with a vanishing statistical mean amplitude. This implies that when the system is initialized around one of the hot spots, the time crystal phase will exist in a prethermal state for a certain time before mixing by quantum fluctuations [54, 55]. Crucially, however, the statistical mixture is composed only of subharmonic states and the system can therefore only tunnel between time-crystalline phases akin to the closed system. The distributions shown in Fig. 2(d) and (e) are therefore involving only symmetry-broken contributions and can be distinguished from featureless thermal distributions, such as shown in Fig. 2(c), by correlation measurements. The study of the dynamics of tunneling events between the hot spots is an interesting topic [58–61] that can characterize the time in which the system remains prethermal, i.e., the intermediate time under which the system fulfills criterion (ii).

IV. SEMICLASSICAL TREATMENT

It is instructive to separate the stationary distributions in Fig. 2 into stationary points (attractors, hot spots) α_j and small fluctuations δa_j away from these points. To this end, we insert a mean-field ansatz $a_j = \alpha_j + \delta a_j$ to our model (2), with coherent states $\alpha_j \equiv \langle a_j \rangle$ and quasiparticle fluctuations $\delta a_j \equiv a_j - \langle a_j \rangle$. We characterize the steady states ($\dot{\alpha}_j = 0$) of the system by solving the resulting mean-field equations of motion [34, 48, 62, 63]

$$\dot{\alpha}_j = i(\Delta_j \alpha_j - V_j \alpha_j^* \alpha_j + G \alpha_j^* - \sum_{k \neq j} J_{jk} \alpha_k) - \frac{\gamma_j}{2} \alpha_j. \quad (7)$$

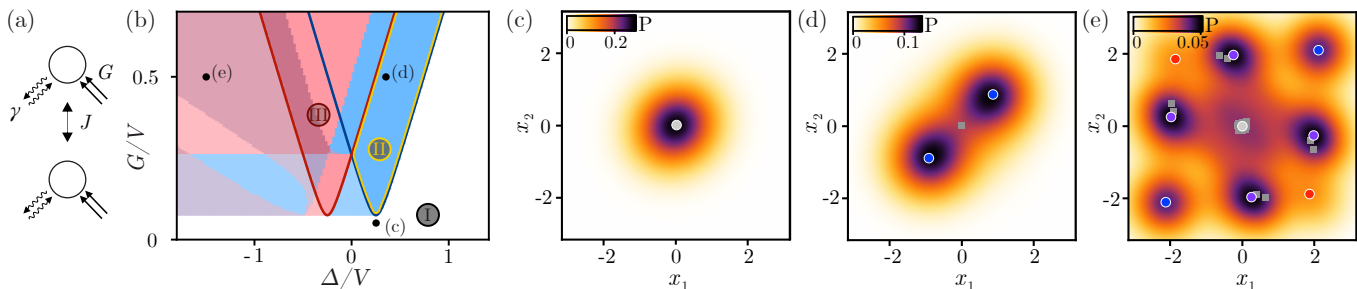


FIG. 2: (a) Network of two identical coupled parametric oscillators. (b) Calculated mean-field stability phase diagram, cf. Eq.(7). White: 0-state is stable; blue: only the S-state is stable; red: S and A-states are stable; purple: S and M-states are stable; dark red: S, A and M-states are stable; Brighter colors: also 0-state is stable. (I-III) indicate the below-threshold regime (I), the simple normal-mode regime (II), and the more complex partial overlapping regime (III) of the instability lobes (marked by blue and red solid lines). (c-e) Probability distribution of the quantum steady state $\langle x_1, x_2 | \rho | x_1, x_2 \rangle$ of measuring (x_1, x_2) simultaneously. Circles indicate the stable mean field steady state solutions and squares indicate the unstable ones, cf. Eq. (7). Their colors indicate their symmetry: blue means symmetric, red means antisymmetric, purple means mixed symmetry and light-gray means 0-amplitude state. (c) Only the 0-amplitude state is occupied. (d) The symmetric states are populated, as they are the only ones with stable mean field solutions. (e) Many states are populated, the M-states are the most probable ones. Parameters are $\kappa/V = 0.1$, $J/V = -0.25$, and detuning and driving strength as shown in (b).

Note that this is equivalent to either employing a saddle-node approximation on a Keldysh action description of the system [48], or solving the corresponding classical system [47].

The resulting semiclassical solutions are located at the hot spots of the projected probability distribution $\langle x_1, x_2 | \rho_s | x_1, x_2 \rangle$, see Fig. 2. We conclude that the mean-field approach identifies the states that contribute most to the unique stationary density matrix ρ_s . In other words, we find that even with very few photons, the stationary density matrix that mixes between the DTTSB quantum states is located around specific ‘hot spots’ in phase space, i.e., at the semiclassical coherent states of the driven system. Thus, we can characterize the phase diagram, as a function of driving strength G and detuning Δ , cf. Refs. [47, 48] and Fig. 2(b). Nevertheless, so far we do not explain the uncertainty distribution around the hot spots nor how the system could ergodically explore the different hot spots in phase space.

Fluctuations – One hallmark of quantum mechanics is the inherent uncertainty accompanying all states in the form of quantum fluctuations. This uncertainty gives rise to the finite probability distribution around the hot spots, see Fig. 2. To account for these fluctuations, we consider the Hamiltonian

$$H_{\text{fl}} = \hbar \sum_k \Omega(\alpha)_{kk} \delta a_k^\dagger \delta a_k + \hbar \sum_{l \neq k} \Omega(\alpha)_{lk} \delta a_l^\dagger \delta a_k + \text{h.c.}, \quad (8)$$

where we neglect terms that are more than bilinear in δa_j , and the prefactors $\Omega(\alpha)$ depend on the specific mean-field solution α . Note that a similar treatment of fluctuations is possible for open systems [48, 62, 64, 65]. In both closed and open cases, the resulting fluctuations describe the dynamics of deviations away from the mean-field solution [48, 65]. The time evolution of the fluctuations is governed by characteristic exponents μ_i that are obtained

by diagonalizing the Hamiltonian or Liouvillian, respectively. Alternatively, they can be read from the poles of the Keldysh Green’s functions [48]. The real and imaginary parts of each μ_i correspond to the typical frequency and decay rate of the fluctuations around a phase of the system, respectively. Note that the fluctuation-induced activation dynamics between phases is not captured by the bilinear description (8), and can be captured, e.g., using an instanton analysis [58–61, 66].

So far, we considered quantum fluctuations in a system coupled to a bath at temperature $T = 0$, cf. Eq. (6) and Fig. 2. In the classical limit of high normal modes’ amplitudes, the influence of these quantum fluctuations rapidly decreases concomitant with a suppression of activation, cf. Appendix A. This results in long prethermal timescales and the DTC remains coherent over a long duration. In the classical limit, significant fluctuations can still enter the system from a high-temperature bath. We refer to this as the thermal limit $k_B T \gg \hbar \omega_0$, where k_B is Boltzmann’s constant. The classical thermal fluctuations, which in contrast to quantum fluctuations can be tuned, should generate similar long-time phenomena with the same characteristic exponents as quantum fluctuations. To test this, we now move to an experimental realization of two coupled parametric oscillators in the presence of classical noise.

V. EXPERIMENTAL REALIZATION

We set out to test if the fluctuation spectra of a time crystal can be observed in a classical experiment. To this end, we study a system of electrical lumped-element RLC resonators that are capacitively coupled. Each resonator is composed of an inductance $L = 87 \mu\text{H}$ and a nonlinear capacitance $C \approx 20 \text{ pF}$ in the form of a dc-biased

varicap diode, see Fig. 3(a). Finite damping enters the system through the electrical resistance, which mostly stems from the contribution of the coil wire. Each resonator is inductively connected to the lock-in amplifier's input and output ports via two auxiliary coils.

Under appropriate driving, each RLC resonator behaves as a KPO. The resonator network can therefore be modeled with Eq. (1) [67]. The parameter values of our resonators are (nearly) identical with eigenfrequencies $\omega_j \approx \omega_0 = 2\pi f_0 = 2\pi \times 2.603$ MHz, $V_j \approx V_0 = 2.56$ μ Hz, and quality factors estimated as $Q_j \approx Q_0 = 233$, leading to homogeneous dissipation coefficients $\gamma_j \approx \gamma_0 = \omega_0/Q_0$. The resonators are driven with the same parametric driving strength $G_j \equiv G = \gamma_0 U_d/(2U_{th})$, where U_d specifies the voltage applied to the driving coil, and $U_{th} = 1.95$ V its threshold for parametric oscillation at $\Delta = 0$. In the following, we discuss experimental results obtained with two resonators with a linear coupling coefficient $J = 0.084$ MHz, placing them in a regime of moderately strong coupling [34, 47].

In previous work, we investigated the steady-state solutions of the coupled system in the Δ - G map [47]. We found a complex phase diagram of time-crystalline solutions with different symmetries. The theoretical analysis of this previous experiment, which is shown in Fig. 2(b), serves as an orientation map in the following discussion. Here, we are interested in the study of fluctuations around the stable solutions of Fig. 2(b). With $T \approx 300$ K, our resonator is deep in the classical limit $\hbar\omega_0 \ll k_B T$. This means that the thermal occupation of $n_{th} \approx 2.5 \times 10^6$ generates a sizeable sampling around the mean-field hot spots, overwhelming the influence of quantum fluctuations. This reiterates the truly classical nature of the physics we measure.

A natural source of classical fluctuations is provided by thermal Johnson noise. However, the room-temperature Johnson noise in our circuit is very small and hard to distinguish from the background noise of the detector (amplifier) noise. Instead, we apply electrical white noise U_{noise} with an approximately white power spectral density S_n . In this way, we mimic the effect of thermal noise at very large temperatures, and measure the resulting fluctuations around various states. The noise enters Eq. (7) as an additional uncorrelated stochastic (Langevin) force $\Xi_{\alpha Re,j} + i\Xi_{\alpha Im,j}$, acting on the real and imaginary axes of the resonators each with power spectral densities $\sigma^2 = \zeta^2/2(\omega_G/2)^2$ [68–70], where $\zeta^2 = 0.0035$ Hz⁴/V² S_n takes into account the signal-in-coupling efficiency and the rotating transformation performed in order to obtain Eq. (7).

VI. EXPERIMENTAL RESULTS

Our experimental procedure is the following: we perform measurements as a function of the driving frequency $f_d = f_0 + \frac{\Delta}{2\pi}$ at a constant driving amplitude $U_d \propto G$. At every value of f_d , we wait until a steady state is

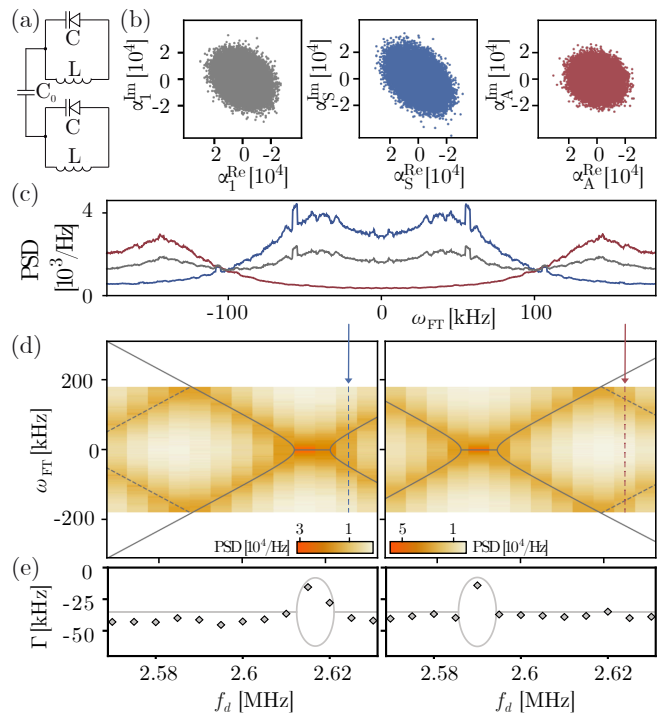


FIG. 3: (a) Experimental setup of two coupled parametric electric resonators. (b) Fluctuations around a stable state involving two coupled parametrons. Shown are the measured oscillations of oscillator 1 (gray), as well as the symmetric (blue) and antisymmetric coordinates (red) calculated from data of both resonators, cf. Eqs. (9) and (10). (c) Measured PSD of oscillator 1 (gray), and of the symmetric (blue) and antisymmetric (red) fluctuations. Fluctuation peaks at different frequencies become visible for the different symmetries. A moving average was used to decrease the point-to-point noise in the PSD. (d) PSD of the symmetric (left) and antisymmetric (right) fluctuations as a function of the driving frequency f_d . The driving strength used here is below threshold, i.e., no DTC appears and the mean amplitudes are zero. Grey lines show the calculated imaginary parts of the characteristic exponents μ , cf. Appendix C. Aliasing appears due to the finite sampling rate [71, 72]. The affected values are indicated by dashed grey lines that are mirrored with respect to the maximum measured frequency. Red and blue dashed vertical lines and arrows mark the position of the measurements presented in (b) and (c). (e) Real parts of the characteristic exponents μ , corresponding to damping; diamonds represent experimental data and lines the theory results. System parameters are $U_d = 1.5$ V, $S_n = 1.1 \times 10^{-9}$ V² Hz⁻¹ and $f_d = 2.605$ MHz.

reached. This steady state corresponds to one of the time-crystalline phases in Fig. 2(b), i.e., a mean-field solution with a certain amplitude and phase for each resonator. Next, we record the fluctuations of each resonator around this stable state in response to the combination of the parametric drive U_d and the noise U_{noise} . To obtain statistically representative data, the measurement time T_{rec} must be much longer than both the lock-in time constant and the resonator ringdown time.

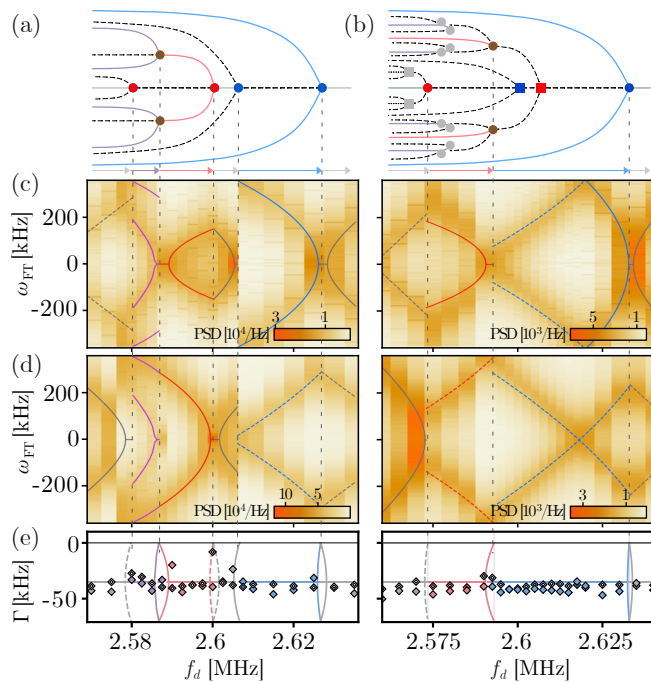


FIG. 4: (a) and (b): bifurcation tree of the experimental system comprising two coupled nonlinear resonators. Solid (dashed) lines indicate stable (unstable) DTC states for driving voltages of $U_d = 4$ V in (a) and $U_d = 6$ V in (b). Dots mark bifurcation points where several solutions emerge/vanish. The higher driving voltage in (b) results in a more complex bifurcation tree due to the larger overlap between the instability lobes, cf. Fig. 2(b). At each value of f_d , the experimental system probes one of the stable solutions, which we color code according to their stationary symmetry: grey (0-amplitude), blue (symmetric), red (anti-symmetric), and purple (mixed-symmetry). As in Fig. 3, we plot the PSD of the (c) symmetric and (d) anti-symmetric fluctuations around the stationary DTC states as a function of the driving frequency f_d , cf. Eqs. (9) and (10). Jumps in the realized DTC solutions are reflected as discontinuities in the measured spectra. We deal with aliasing as explained in the caption of Fig. 3. (e) Real parts of μ , corresponding to damping; diamonds represent experimental data and lines the theory results. $S_n = 1.1 \times 10^{-9} \text{ V}^2 \text{ Hz}^{-1}$ and $f_d = 2.605$ MHz.

For a single, isolated resonator, we can Fourier transform the measured quadrature fluctuations $\delta\alpha^{\text{Re}} = \alpha^{\text{Re}} - \bar{\alpha}^{\text{Re}}$ and $\delta\alpha^{\text{Im}} = \alpha^{\text{Im}} - \bar{\alpha}^{\text{Im}}$, where bars indicate the mean values (steady states). These fluctuations around the mean values are similar to thermal oscillations of a harmonic oscillator but around a displaced frame. The position and width of the fluctuation peaks in the resulting spectrum allow us to extract the fluctuation frequency ω_{FT} and decay rate Γ , see Appendix B.

For coupled resonators, the fluctuations around the stable states are themselves coupled and form normal modes, see Fig. 3(b). As we measure the response of both resonators individually, we can analyze the fluctuations in terms of their symmetric and antisymmetric

normal-mode components, which are defined as

$$\delta\alpha_{S,A}^{\text{Re}} = (\delta\alpha_1^{\text{Re}} \pm \delta\alpha_2^{\text{Re}})/\sqrt{2}, \quad (9)$$

$$\delta\alpha_{S,A}^{\text{Im}} = (\delta\alpha_1^{\text{Im}} \pm \delta\alpha_2^{\text{Im}})/\sqrt{2}. \quad (10)$$

We emphasize that the symmetries of the fluctuations are independent of the symmetries of the selected steady states. The former are observed as perturbations within the frame rotating at the frequency of the latter. For instance, the fluctuations around a symmetrical normal-mode steady state exhibit both symmetric and antisymmetric components. In general, these components appear at different frequencies ω_{FT} , which allows us to distinguish them in the Fourier transform of the corresponding coordinate, see Fig. 3(c).

As a starting point, we probe the fluctuations of the coupled system as a function of f_d below the parametric threshold, i.e., at small driving U_d where no time-crystalline phases exist. This corresponds to a horizontal cut through regime I, cf. Fig. 2(b). In Fig. 3(b), we display the fluctuations of resonator 1 in its own coordinates α^{Re} and α^{Im} , as well as the symmetric and antisymmetric fluctuation of both resonators. Since we are below threshold, $\bar{\alpha}_i = 0$, and we can identify $\delta\alpha_i = \alpha_i$ in this case. For detunings Δ close to the symmetric instability lobe, we observe an elongated (squeezed) phase space distribution for α_S , while α_A remains round [64]. The corresponding power spectral densities (PSD) are shown in Fig. 3(c), demonstrating the different frequencies of the symmetric and antisymmetric fluctuations. Note that both are far below the resonance frequency $f_0 = 2.603$ MHz.

In Fig. 3(d) and (e), we summarize the PSDs of the fluctuations measured at different frequencies, and compare them to the values calculated with our analytic prediction for the characteristic exponents μ_i , cf. Appendix C. The predicted fluctuation frequencies and bandwidths match those of the measured PSDs. In particular, we observe regions where the fluctuations have a well-defined frequency and lifetime. At other points, the frequencies go to zero while the decay rate splits due to the phase-dependent parametric amplification [48, 73]. The eigenvalue diagram is similar to that of a damped harmonic resonator going from an underdamped to an overdamped motion at a so-called ‘exceptional point’ [48]. We note that multiple such scenarios emerge in our network.

For $U_d > U_{th}$, the driving is sufficiently strong to generate DTCs in a certain frequency range. In Fig. 4, we explore the fluctuations in this regime for two different values of U_d . The two sweeps represent cuts through the diagram in Fig. 2(b) below and above the point where the two instability lobes start to overlap, respectively. In general, the system possesses a multitude of stable states with a complex bifurcation tree, see Fig. 4(a) and (b). The experiment samples one particular oscillation state at each frequency. Hence, the experimental sweeps follow trajectories along the bifurcation diagram, see Figs. 4(c) to (e). A jump between different states, typically at a

bifurcation point, causes a jump in the measured fluctuation spectrum [75]. Several such jumps can be observed in our measurements. Again, all measured spectra can be modeled using the characteristic exponents μ_i , in spite of the fact that our devices are deep in the classical regime. The main difference between the closed and open cases involves the finite lifetime of the fluctuations, see Fig. 4(e).

VII. DISCUSSION AND OUTLOOK

Our results demonstrate that quantum DTC physics has a clear connection to classical periodic-doubling bifurcations [28, 32]. In our analysis, we showcase that both the quantum and classical limits stem from the same model description and exhibit the same mean-field order parameters as well as fluctuations. We therefore establish that the criterion (ii) delineated as a requirement for DTCs is solely maintained within prethermal timescales [3, 44, 45]. We further highlight how different parts of a closed system can act as an effective bath to the normal modes that undergo DTTSB, thus unifying the description for both coherent and dissipative DTCs. As classical systems with massive mode population are resilient to fluctuations, they have diverging prethermal timescales, making them superior to their quantum counterparts. This allows us to understand current realizations of quantum DTCs [1–3, 6, 19–21] as a continuation of earlier accounts of DTTSB, see e.g., Ref. [29].

Our study relies on a specific model that maps to our classical experiment. Nonetheless, we emphasize that the physics seen should be applicable to a wide range of interacting systems, including DTCs in many-body localized systems. In particular, the similarity between the effects of quantum and classical fluctuations, and the requirements for stability in the thermodynamic limit, are generally evident. To summarize, our work on a parametrically driven-dissipative system clarifies many contentious issues in the exciting frontier of discrete time crystals, showing that there is no fundamental distinction between classical and quantum time-crystalline phases.

Acknowledgments

This work received financial support from the Swiss National Science Foundation through grants (CR-SII5.177198/1) and (PP00P2.190078), and from the Deutsche Forschungsgemeinschaft (DFG) - project number 449653034. We thank Peter Märki and Žiga Nosan for technical help.

Appendix A: Classical system

The classical version of Eq. (1) corresponds to a coupled parametric oscillator network [Eq. (1)] and is de-

scribed by the following equation of motion [61]:

$$\ddot{x}_j + \omega_j^2(1 - \lambda \cos \omega_G t)x_j + A_j x_j^3 + \sum_{k \neq j} J_{jk} \sqrt{\omega_j \omega_k} x_k, \quad (\text{A1})$$

where the parametric driving is related to the two-photon drive via $\lambda = 4G/\omega_j$, and the Duffing-nonlinearity to the Kerr-nonlinearity via $A_j = 4\omega_j^2 V_j/3\hbar$. Note the explicit dependence on \hbar in the latter relation because of the nonlinearity. In the classical limit $\hbar \rightarrow 0$, the high amplitudes [$a \sim 1/\sqrt{\hbar}$] cancels the \hbar in A_j . The description of the classical system can be simplified analogously to the quantum system by going into a rotating frame at $\omega_G/2$ and neglecting fast oscillating terms yielding equations corresponding to the mean-field equations for α_j , Eq. (7) [34, 62, 63].

Appendix B: Single resonator

In the following we present our fluctuation analysis for a single oscillator. Fig. 5(a) shows the measured fluctuations around a stable state (with 0-amplitude in this case). The corresponding PSD [Fig. 5(b)] can be used to identify the fluctuation frequency (peak frequency) and the decay rate (peak width) by using the best fit for Eq. (C3). Repeating the procedure we can study their dependence on the driving frequency f_d [Fig. 5(f) and (g)]. We do this for driving strengths above and below threshold. Below threshold only the stable state at 0 amplitude is available. When the driving frequency f_d approaches f_0 , the fluctuation frequency vanishes, while the decay rate Γ splits, i.e. the fluctuations are overdamped [48]. For increased driving strength, the system hosts phase states at higher amplitudes. We analogously measure their fluctuation spectrum and find that the fluctuation frequency vanishes, when the system transitions from the 0-amplitude state to the high amplitude phase state. At the same time, the decay time splits and one value approaches 0 at the transition. For a broad range away from the transition, the decay time is constant at $\Gamma = \gamma_0/2$, fixed by the dissipation coefficient γ_0 .

Appendix C: Derivation of the PSD

In the following we will derive the power spectral density (PSD) of small fluctuations around a stable state. It describes the noise-induced motion around the stable states presented in Figs. 3 and 4. The small fluctuation can be well described by linearizing the equations of motion (7) around the steady state. The noisy system is then described by

$$\delta \dot{\mathbf{Y}} = M_J \delta \mathbf{Y} + \boldsymbol{\Xi}, \quad (\text{C1})$$

where $\delta \mathbf{Y} = (\delta \alpha_1^{\text{Re}}, \delta \alpha_1^{\text{Im}}, \delta \alpha_2^{\text{Re}}, \dots, \delta \alpha_N^{\text{Re}})$ with $\delta \alpha_j = \langle \delta \hat{a}_j \rangle$, M_J is the Jacobian matrix of the right side of

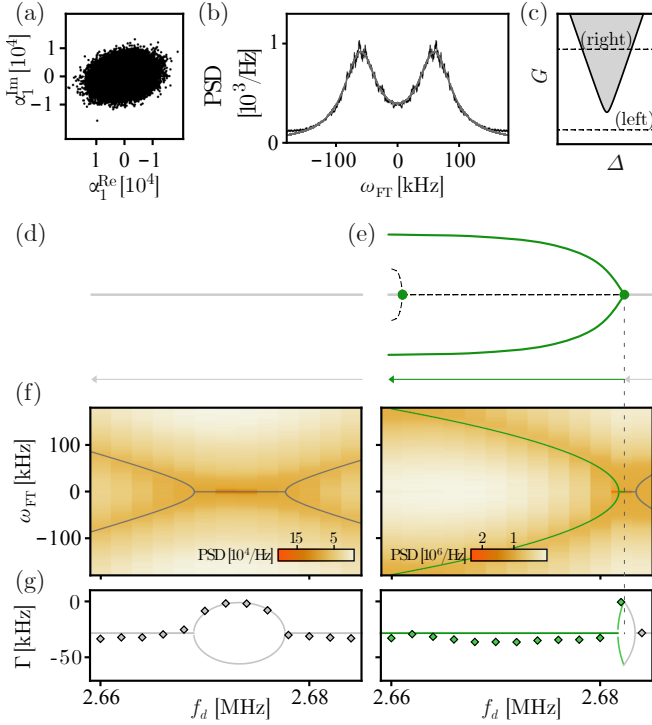


FIG. 5: Fluctuations around stable states in a single parametron. (a) Measured fluctuation around the origin for $U_d = 1.3$ V, $S_n = 1.1 \times 10^{-9}$ V² Hz⁻¹ and $f_d = 2.684$ MHz. (b) Power spectral density (PSD) of the fluctuations (black) and fit (gray). (c) Sketch of the parametric driving strength applied for the right and the left panel w.r.t. the instability lobe. (d) and (e): bifurcation tree of the single nonlinear resonators. Solid (dashed) lines indicate stable (unstable) DTC states for driving voltages (d) below and (e) above threshold. Dots mark bifurcation points. At each value of f_d , the experimental system probes one of the stable solutions, which we color code: grey (0-amplitude) and green (high-amplitude phase state). (f) Measured PSD of the fluctuations around the stationary DTC states as a function of the driving frequency f_d . Solid lines show the imaginary parts of the characteristic exponent μ . (g) Real parts of μ , corresponding to damping; diamonds represent experimental data and lines the theory results. System parameters: $Q = 295$, $f_0 = 2.6733$ MHz, $U_{th} = 1.35$ V, and U_d is 1.3 V (left panel) and 3 V (right panel).

Eq. (7) evaluated at the coordinates of the selected solution $\mathbf{Y}_s = (\alpha_{1,s}^{\text{Re}}, \alpha_{1,s}^{\text{Im}}, \dots, \alpha_{N,s}^{\text{Im}})$ [48, 62, 64, 65], and the vector Ξ contains $2N$ uncorrelated white noise processes with PSD σ^2 . The time evolution of the eigenvector components is then governed by $e^{\mu_i t}$, where the characteristic exponent μ_i is the i^{th} eigenvalue of the Jacobian matrix M_J . A state \mathbf{Y}_s is stable if and only if the real parts of all eigenvalues are negative. Furthermore, the real and imaginary parts of each μ_i correspond to the typical frequency and decay rate Γ of the fluctuations around a stable state, respectively.

Fourier transforming the Langevin equation (C1) yields

$$-i\omega_{\text{FT}}\delta\mathbf{Y}(\omega_{\text{FT}}) = M_J\delta\mathbf{Y}(\omega_{\text{FT}}) + \Xi(\omega_{\text{FT}}). \quad (\text{C2})$$

We solve for the Fourier components $\mathbf{Y}(\omega_{\text{FT}})$ and calculate the PSD of δY_i by $|\delta Y_i(\omega_{\text{FT}})|^2$ using the PSD of the noise processes $\Xi(\omega_{\text{FT}})$. The same can also be done for the symmetric and anti-symmetric coordinates. In the experiment we used two coupled parametric oscillators, thus M_J is a 4×4 matrix, which we can diagonalize. Using the symmetries of M_J we find the eigenvalues μ_j and the corresponding eigenvectors $w_j \otimes (e_j, 1)$ with $w_j = (1, 1)$ for $j = 1, 2$ and $w_j = (1, -1)$ for $j = 3, 4$. We can now express the PSD as a function of μ_j and e_j and obtain $\text{PSD}_j = \text{PSD}_{\alpha_j^{\text{Re}}} + \text{PSD}_{\alpha_j^{\text{Im}}}$. Each PSD is given by

$$\text{PSD}_j = \frac{\sigma^2 \left(\text{Im}(\mu_j)^2 \left(2\text{Im}(e_j)^2 \text{Re}(e_j)^2 + \text{Im}(e_j)^4 + (\text{Re}(e_j)^2 + 1)^2 \right) + 2\text{Im}(e_j)^2 (\text{Re}(\mu_j)^2 + \omega^2) \right)}{\text{Im}(e_j)^2 \left((\text{Im}(\mu_j)^2 - \omega^2)^2 + \text{Re}(\mu_j)^2 (2\text{Im}(\mu_j)^2 + \text{Re}(\mu_j)^2 + 2\omega^2) \right)}. \quad (\text{C3})$$

This simple form holds true whenever the corresponding eigenvalue μ_j appears in complex conjugated pairs, but

also gives very good results for real-valued μ_j .

- [2] D. V. Else, B. Bauer, and C. Nayak, Floquet time crystals, *Phys. Rev. Lett.* **117**, 090402 (2016).
- [3] D. V. Else, B. Bauer, and C. Nayak, Prethermal phases of matter protected by time-translation symmetry, *Phys. Rev. X* **7**, 011026 (2017).
- [4] C. W. von Keyserlingk and S. L. Sondhi, Phase structure of one-dimensional interacting floquet systems. ii. symmetry-broken phases, *Phys. Rev. B* **93**, 245146 (2016).
- [5] C. W. von Keyserlingk, V. Khemani, and S. L. Sondhi, Absolute stability and spatiotemporal long-range order in floquet systems, *Phys. Rev. B* **94**, 085112 (2016).
- [6] N. Y. Yao, A. C. Potter, I.-D. Potirniche, and A. Vishwanath, Discrete time crystals: Rigidity, criticality, and realizations, *Phys. Rev. Lett.* **118**, 030401 (2017).
- [7] J. Zhang, P. W. Hess, A. Kyprianidis, P. Becker, A. Lee, J. Smith, G. Pagano, I.-D. Potirniche, A. C. Potter, A. Vishwanath, N. Y. Yao, and C. Monroe, Observation of a discrete time crystal, *Nature* **543**, 217 (2017).
- [8] S. Choi, J. Choi, R. Landig, G. Kucsko, H. Zhou, J. Isoya, F. Jelezko, S. Onoda, H. Sumiya, V. Khemani, C. von Keyserlingk, N. Y. Yao, E. Demler, and M. D. Lukin, Observation of discrete time-crystalline order in a disordered dipolar many-body system, *Nature* **543**, 221 (2017).
- [9] W. W. Ho, S. Choi, M. D. Lukin, and D. A. Abanin, Critical time crystals in dipolar systems, *Phys. Rev. Lett.* **119**, 010602 (2017).
- [10] K. Sacha and J. Zakrzewski, Time crystals: a review, *Reports on Progress in Physics* **81**, 016401 (2017).
- [11] M. I. Dykman, C. Bruder, N. Lörch, and Y. Zhang, Interaction-induced time-symmetry breaking in driven quantum oscillators, *Phys. Rev. B* **98**, 195444 (2018).
- [12] J. Rovny, R. L. Blum, and S. E. Barrett, ³¹P nmr study of discrete time-crystalline signatures in an ordered crystal of ammonium dihydrogen phosphate, *Phys. Rev. B* **97**, 184301 (2018).
- [13] W. Berdanier, M. Kolodrubetz, S. A. Parameswaran, and R. Vasseur, Floquet quantum criticality, *Proceedings of the National Academy of Sciences* **115**, 9491 (2018).
- [14] N. Y. Yao and C. Nayak, Time crystals in periodically driven systems, *Physics Today* **71**, 40 (2018).
- [15] A. Russomanno, F. Iemini, M. Dalmonte, and R. Fazio, Floquet time crystal in the lipkin-meshkov-glick model, *Phys. Rev. B* **95**, 214307 (2017).
- [16] B. Buča, J. Tindall, and D. Jaksch, Non-stationary coherent quantum many-body dynamics through dissipation, *Nature Communications* **10**, 1730 (2019).
- [17] K. Giergiel, T. Tran, A. Zaheer, A. Singh, A. Sidorov, K. Sacha, and P. Hannaford, Creating big time crystals with ultracold atoms, *New Journal of Physics* **22**, 085004 (2020).
- [18] A. Pizzi, J. Knolle, and A. Nunnenkamp, Higher-order and fractional discrete time crystals in clean long-range interacting systems, *Nature Communications* **12**, 2341 (2021).
- [19] J. Randall, C. E. Bradley, F. V. van der Gronden, A. Galicia, M. H. Abobeih, M. Markham, D. J. Twitchen, F. Machado, N. Y. Yao, and T. H. Taminiau, Many-body-localized discrete time crystal with a programmable spin-based quantum simulator, *Science* **0**, eabk0603 (2021), <https://www.science.org/doi/pdf/10.1126/science.abk0603>.
- [20] M. Ippoliti, K. Kechedzhi, R. Moessner, S. Sondhi, and V. Khemani, Many-body physics in the nisq era: Quantum programming a discrete time crystal, *PRX Quantum* **2**, 030346 (2021).
- [21] X. Mi, M. Ippoliti, C. Quintana, A. Greene, Z. Chen, J. Gross, F. Arute, K. Arya, J. Atalaya, R. Babush, J. C. Bardin, J. Basso, A. Bengtsson, A. Bilmes, A. Bourassa, L. Brill, M. Broughton, B. B. Buckley, D. A. Buell, B. Burkett, N. Bushnell, B. Chiaro, R. Collins, W. Courtney, D. Debroy, S. Demura, A. R. Derk, A. Dunsworth, D. Eppens, C. Erickson, E. Farhi, A. G. Fowler, B. Foxen, C. Gidney, M. Giustina, M. P. Harrigan, S. D. Harrington, J. Hilton, A. Ho, S. Hong, T. Huang, A. Huff, W. J. Huggins, L. B. Ioffe, S. V. Isakov, J. Iveland, E. Jeffrey, Z. Jiang, C. Jones, D. Kafri, T. Khattar, S. Kim, A. Kitaev, P. V. Klimov, A. N. Korotkov, F. Kostritsa, D. Landhuis, P. Laptev, J. Lee, K. Lee, A. Locharla, E. Lucero, O. Martin, J. R. McClean, T. McCourt, M. McEwen, K. C. Miao, M. Mohseni, S. Montazeri, W. Mruczkiewicz, O. Naaman, M. Neeley, C. Neill, M. Newman, M. Y. Niu, T. E. O'Brien, A. Opremcak, E. Ostby, B. Pato, A. Petukhov, N. C. Rubin, D. Sank, K. J. Satzinger, V. Shvarts, Y. Su, D. Strain, M. Szalay, M. D. Trevithick, B. Villalonga, T. White, Z. J. Yao, P. Yeh, J. Yoo, A. Zalcman, H. Neven, S. Boixo, V. Smelyanskiy, A. Megrant, J. Kelly, Y. Chen, S. L. Sondhi, R. Moessner, K. Kechedzhi, V. Khemani, and P. Roushan, Time-Crystalline Eigenstate Order on a Quantum Processor, *Nature* [10.1038/s41586-021-04257-w](https://doi.org/10.1038/s41586-021-04257-w) (2021).
- [22] B. Huang, Y.-H. Wu, and W. V. Liu, Clean floquet time crystals: Models and realizations in cold atoms, *Phys. Rev. Lett.* **120**, 110603 (2018).
- [23] S. Autti, V. B. Eltsov, and G. E. Volovik, Observation of a time quasicrystal and its transition to a superfluid time crystal, *Phys. Rev. Lett.* **120**, 215301 (2018).
- [24] K. Giergiel, A. Dauphin, M. Lewenstein, J. Zakrzewski, and K. Sacha, Topological time crystals, *New Journal of Physics* **21**, 052003 (2019).
- [25] D. V. Else, C. Monroe, C. Nayak, and N. Y. Yao, Discrete time crystals, *Annual Review of Condensed Matter Physics* **11**, 467 (2020), <https://doi.org/10.1146/annurev-conmatphys-031119-050658>.
- [26] J. Smits, L. Liao, H. T. C. Stoof, and P. van der Straten, Observation of a space-time crystal in a superfluid quantum gas, *Phys. Rev. Lett.* **121**, 185301 (2018).
- [27] J. Smits, H. T. C. Stoof, and P. van der Straten, On the long-term stability of space-time crystals, *New Journal of Physics* **22**, 105001 (2020).
- [28] L. Landau and E. Lifshitz, *Mechanics*, Butterworth-Heinemann (1976).
- [29] M. Faraday, On a peculiar class of acoustical figures; and on certain forms assumed by groups of particles upon vibrating elastic surfaces, *Philosophical transactions of the Royal Society of London* **121**, 299 (1831).
- [30] E. Mathieu, E. mathieu. — mémoire sur le mouvement vibratoire des cloches (journal de l'école polytechnique, lie cahier, 1882), *J. Phys. Theor. Appl.* **2**, 32 (1883).
- [31] L. Rayleigh, Xvii. on the maintenance of vibrations by forces of double frequency, and on the propagation of waves through a medium endowed with a periodic structure, *The London, Edinburgh, and Dublin Philosophical Magazine and Journal of Science* **24**, 145 (1887).
- [32] A. H. Nayfeh and D. T. Mook, *Nonlinear Oscillations*, Physics textbook (Wiley, 2008).

- [33] M. Dykman, *Fluctuating Nonlinear Oscillators* (Oxford University Press, 2012).
- [34] T. L. Heugel, M. Oscity, A. Eichler, O. Zilberberg, and R. Chitra, Classical many-body time crystals, *Phys. Rev. Lett.* **123**, 124301 (2019).
- [35] F. M. Gambetta, F. Carollo, M. Marcuzzi, J. P. Garrahan, and I. Lesanovsky, Discrete time crystals in the absence of manifest symmetries or disorder in open quantum systems, *Phys. Rev. Lett.* **122**, 015701 (2019).
- [36] Z. Gong, R. Hamazaki, and M. Ueda, Discrete time-crystalline order in cavity and circuit qed systems, *Phys. Rev. Lett.* **120**, 040404 (2018).
- [37] B. Zhu, J. Marino, N. Y. Yao, M. D. Lukin, and E. A. Demler, Dicke time crystals in driven-dissipative quantum many-body systems, *New Journal of Physics* **21**, 073028 (2019).
- [38] A. Lazarides, S. Roy, F. Piazza, and R. Moessner, Time crystallinity in dissipative floquet systems, *Phys. Rev. Research* **2**, 022002 (2020).
- [39] A. Riera-Campeny, M. Moreno-Cardoner, and A. Sanpera, Time crystallinity in open quantum systems, *Quantum* **4**, 270 (2020).
- [40] H. Keßler, P. Kongkhambut, C. Georges, L. Mathey, J. G. Cosme, and A. Hemmerich, Observation of a dissipative time crystal, *Phys. Rev. Lett.* **127**, 043602 (2021).
- [41] V. Savona, Spontaneous symmetry breaking in a quadratically driven nonlinear photonic lattice, *Phys. Rev. A* **96**, 033826 (2017).
- [42] R. Rota, F. Minganti, C. Ciuti, and V. Savona, Quantum critical regime in a quadratically driven nonlinear photonic lattice, *Phys. Rev. Lett.* **122**, 110405 (2019).
- [43] T. L. Heugel, M. Biondi, O. Zilberberg, and R. Chitra, Quantum transducer using a parametric driven-dissipative phase transition, *Phys. Rev. Lett.* **123**, 173601 (2019).
- [44] A. Pizzi, A. Nunnenkamp, and J. Knolle, Classical approaches to prethermal discrete time crystals in one, two, and three dimensions, *Phys. Rev. B* **104**, 094308 (2021).
- [45] A. Pizzi, A. Nunnenkamp, and J. Knolle, Classical prethermal phases of matter, *Phys. Rev. Lett.* **127**, 140602 (2021).
- [46] J. Kořata, A. Leuch, T. Kästli, and O. Zilberberg, Fixing the rotating-wave approximation for strongly-detuned quantum oscillators, arXiv preprint at arXiv:2202.13172 (2022).
- [47] T. L. Heugel, O. Zilberberg, C. Marty, R. Chitra, and A. Eichler, Ising machines with strong bilinear coupling, *Phys. Rev. Research* **4**, 013149 (2022).
- [48] M. Soriente, T. L. Heugel, K. Arimitsu, R. Chitra, and O. Zilberberg, Distinctive class of dissipation-induced phase transitions and their universal characteristics, *Phys. Rev. Research* **3**, 023100 (2021).
- [49] A. M. Perelomov and V. S. Popov, Group-theoretical aspects of the variable frequency oscillator problem, *Theoretical and Mathematical Physics* **1**, 275 (1969).
- [50] C. Zerbe and P. Hänggi, Brownian parametric quantum oscillator with dissipation, *Phys. Rev. E* **52**, 1533 (1995).
- [51] C. Stambaugh and H. B. Chan, Noise-activated switching in a driven nonlinear micromechanical oscillator, *Phys. Rev. B* **73**, 172302 (2006).
- [52] H. B. Chan and C. Stambaugh, Activation barrier scaling and crossover for noise-induced switching in micromechanical parametric oscillators, *Phys. Rev. Lett.* **99**, 060601 (2007).
- [53] N. Y. Yao, C. Nayak, L. Balents, and M. P. Zaletel, Classical discrete time crystals, *Nature Physics* **16**, 438 (2020).
- [54] A. Grimm, N. E. Frattini, S. Puri, S. O. Mundhada, S. Touzard, M. Mirrahimi, S. M. Girvin, S. Shankar, and M. H. Devoret, Stabilization and operation of a kerr-cat qubit, *Nature* **584**, 205 (2019).
- [55] F. Minganti, N. Bartolo, J. Lolli, W. Casteels, and C. Ciuti, Exact results for Schrödinger cats in driven-dissipative systems and their feedback control, *Sci. Rep.* **6**, 26987 (2016).
- [56] N. McLachlan, *Theory and application of Mathieu functions* (Clarendon, 1951).
- [57] J. Johansson, P. Nation, and F. Nori, Qutip 2: A python framework for the dynamics of open quantum systems, *Computer Physics Communications* **184**, 1234 (2013).
- [58] G. Margiani, S. Guerrero, T. L. Heugel, C. Marty, R. Pachlatko, T. Gisler, G. D. Vukasin, H.-K. Kwon, J. M. Miller, N. E. Bousse, T. W. Kenny, O. Zilberberg, D. Sabonis, and A. Eichler, Fluctuating trajectories and switching rates of a synthetic two-level system, arXiv preprint at arXiv:2112.03357 (2022).
- [59] P. Kinsler and P. D. Drummond, Quantum dynamics of the parametric oscillator, *Phys. Rev. A* **43**, 6194 (1991).
- [60] B. Wielinga and G. J. Milburn, Quantum tunneling in a kerr medium with parametric pumping, *Phys. Rev. A* **48**, 2494 (1993).
- [61] M. Marthaler and M. I. Dykman, Switching via quantum activation: A parametrically modulated oscillator, *Phys. Rev. A* **73**, 042108 (2006).
- [62] J. Guckenheimer and P. Holmes, *Nonlinear oscillations, dynamical systems, and bifurcations of vector fields*, Applied mathematical sciences (Springer-Verlag, 1990).
- [63] L. Papariello, O. Zilberberg, A. Eichler, and R. Chitra, Ultrasensitive hysteretic force sensing with parametric nonlinear oscillators, *Phys. Rev. E* **94**, 022201 (2016).
- [64] J. S. Huber, G. Rastelli, M. J. Seitner, J. Kölbl, W. Belzig, M. I. Dykman, and E. M. Weig, Spectral evidence of squeezing of a weakly damped driven nanomechanical mode, *Phys. Rev. X* **10**, 021066 (2020).
- [65] M. Soriente, R. Chitra, and O. Zilberberg, Distinguishing phases using the dynamical response of driven-dissipative light-matter systems, *Phys. Rev. A* **101**, 023823 (2020).
- [66] F. Thompson and A. Kamenev, Qubit decoherence and symmetry restoration through real-time instantons, arXiv preprint at arXiv:2111.10433 (2021).
- [67] Z. Nosan, P. Märki, N. Hauff, C. Knaut, and A. Eichler, Gate-controlled phase switching in a parametron, *Phys. Rev. E* **99**, 062205 (2019).
- [68] R. Z. Khas'minskii, A limit theorem for the solutions of differential equations with random right-hand sides, *Theory of Probability & Its Applications* **11**, 390 (1966), <https://doi.org/10.1137/1111038> .
- [69] J. Roberts and P. Spanos, Stochastic averaging: An approximate method of solving random vibration problems, *International Journal of Non-Linear Mechanics* **21**, 111 (1986).
- [70] A. Eichler, T. L. Heugel, A. Leuch, C. L. Degen, R. Chitra, and O. Zilberberg, A parametric symmetry breaking transducer, *Applied Physics Letters* **112**, 233105 (2018), <https://doi.org/10.1063/1.5031058> .
- [71] H. Nyquist, Certain topics in telegraph transmission theory, *Transactions of the American Institute of Electrical Engineers* **47**, 617 (1928).

- [72] C. Shannon, Communication in the presence of noise, [Proceedings of the IRE](#) **37**, 10 (1949).
- [73] F. Ferri, R. Rosa-Medina, F. Finger, N. Dogra, M. Sori-ente, O. Zilberberg, T. Donner, and T. Esslinger, Emerging dissipative phases in a superradiant quantum gas with tunable decay, [Phys. Rev. X](#) **11**, 041046 (2021).
- [74] If this state transition happens continuously, also the fluctuation frequency and the decay time change continuously. Commonly, right before the transition, either the symmetric or the antisymmetric fluctuations become overdamped, signaling the upcoming instability of the solution.
- [75] If this state transition happens continuously, also the fluctuation frequency and the decay time change continuously. Commonly, right before the transition, either the symmetric or the antisymmetric fluctuations become overdamped, signaling the upcoming instability of the solution.